JOURNAL OF PROPULSION AND POWER
Vol. 23, No. 5, September–October 2007

Modeling Jet Engine Aerosols in the Postcombustor Flow Path and Sampling System

Thomas Wey* and Nan-Suey Liu†
NASA John H. Glenn Research Center at Lewis Field, Cleveland, Ohio 44135

DOI: 10.2514/1.24274

Aircraft emissions contribute to climate change in the atmosphere and air pollution in the neighborhood of airports. Assessment of the magnitude of the environmental impact of these emissions calls for the combined use of measurements and modeling studies. This paper addresses the use of a computational-fluid-dynamics-based modeling and simulation tool that accounts for and integrates fluid dynamics, chemistry, and particle microphysics relevant to aircraft emissions. The models include sulfate and nitrate aerosol precursors, thermophoresis, coagulation, nucleation, soot activation, condensation/evaporation, and interaction between the gaseous species and the particles. The current capabilities are demonstrated by the results of several applications: the first stage of a high-pressure turbine, the sampling probes, the sampling lines, and a pressure-reduction chamber. They indicate that this modeling and simulation tool can be used to complement the experimental studies as well as to assist the development of sampling and measurement methodology for particle emissions.

Nomenclature

A = control surface
$B_{k,j}$ = coagulation kernel or collision frequency function of two colliding particles, m^3/particle/s
C = molar density of a gaseous species, mol/m^3
Cc_i = Cunningham slip factor
C_{crit} = minimum mass concentration of gaseous H_2SO_4 to decide whether H_2SO_4–H_2O nucleation commences, μg m^{-3}
C_u = turbulent constant, 0.009
$\bar{c}$ = mean thermal speed for SO_3
c_m = isothermal slip coefficient, 1.0
$\bar{c}_m$ = mean thermal velocity of gaseous species m
$\bar{c}_{p,i}$ = mean thermal speed of a particle in size bin i
c_t = temperature jump coefficient, 2.2
D_{eff} = effective mass diffusivity coefficient, $(\mu_t + \mu)/\rho Sc$
D_M = effective molecular (Brownian) diffusivity coefficient
$D_{p,i}$ = particle diffusion coefficient in the ith size bin
$D_{p,j}$ = particle diffusion coefficient in the jth size bin
$D_{v,m}$ = diffusivity of species m
$D^*_{v,m,k}$ = modified diffusivity
d_i = diameter of particles in the ith size bin
d_j = diameter of particles in the jth size bin
$d_{p,g}$ = median diameter of particles, m
$d_{p,k}$ = diameter of the particles in size bin k
E = total energy density
$f_{i,j,k}$ = bin partitioning function
f_u = damping function of the turbulence model
h = computational fluid dynamics time step used in the solution of the carrier gas
J_{hom} = homogeneous nucleation rate, particle/m^3/s
Kn_i = Knudsen number for a particle in size bin i
k = turbulent kinetic energy
k_B = Boltzmann constant, 1.380658×10^{-23} J/K/molecule
k_g = gas thermal conductivities
k_p = particle thermal conductivities
M_B = total number of the size bins
m_i = mass of a particle in size bin i
N_k = number density of particles in size bin k
N_T = number of size distributions
N_{total} = total number of particles of all sizes per cubic meter of the exhaust gas
p = static pressure
$\boldsymbol{q}$ = heat flux vector
R_u = universal gas constant
Sc = gas Schmidt number
S_k = source term for k
S_ε = source term for ε
T = absolute temperature, K
T_1 = production of larger particles from self-coagulation and from heterocoagulation
T_2 = production of particles from heterocoagulation among the other two independent distributions
T_3 = self-coagulation loss
$\boldsymbol{U}_g$ = grid velocity
$\boldsymbol{u}$ = flow velocity in a stationary Cartesian coordinate system
V = control volume
$\boldsymbol{V}_{\text{TH}_k}$ = thermophoretic velocity of a particle in size bin k
$\dot{w}'''_m$ = production rate of species m per unit volume
α = mass accommodation coefficient, sticking probability
ΔG^* = change of the Gibbs free energy during the phase change, J/mol
δ_i = correction factor
ε = turbulent dissipation rate
θ_i = fraction of soot surface activation in size bin i
κ = thermal conductivity
μ = laminar viscosity
μ_g = dynamic viscosity of the carrier gas
μ_t = turbulent viscosity
ν_t = turbulent kinematic viscosity
ρ = fluid density
ρ_m = partial density of species m
σ_g = geometric standard deviation
σ_0 = average number of sites per unit area of soot surface ($\sigma_0 \approx 5 \times 10^{18}$ m^{-2})
τ = viscous stress tensor
υ_k = volume of a particle in size bin k
$\boldsymbol{\omega}_g$ = grid rotating velocity for each designated axis

Received 27 March 2006; revision received 22 February 2007; accepted for publication 28 March 2007.

*Currently Senior Research Scientist, Taitech, Inc.
†Aerospace Engineer, Combustion Branch. Associate Fellow AIAA.

I. Introduction

ALTHOUGH much is still uncertain about the magnitudes of their impact, aircraft emissions can influence climate change in the atmosphere [1] as well as health responses in the vicinity of airports [2]. To alleviate these increasingly significant impacts on the environment, it is necessary to acquire a better understanding of the formation and the subsequent development of gaseous pollutants, aerosols (volatile particles and soot), and their precursors in the internal flow and in the plume of the jet engines operating over the full range from ground to flight altitude. This has been conducted through efforts that combine the use of measurements and low-order modeling studies [3–5]. This paper addresses the use of higher-fidelity modeling and simulation to complement the experimental studies and to assist the development of sampling and measurement methodology for particle emissions.

The volatile nature of aerosols introduces difficulties in their repeatable and accurate measurement, because their concentration and size can be quite sensitive to the sampling conditions and procedures. These difficulties are sometimes further compounded by the necessity of in situ measurements, that is, sampling from aircraft in flight. Clearly, the ability to predict the effects of sampling conditions and procedures on the aerosol behavior will greatly assist the development of sampling techniques and the optimization of sampling procedures for making quantitatively accurate measurements of particulate emissions.

Current modeling studies often have used low-order methods in which chemical kinetics and/or particle microphysics are driven by averaged flow parameters specified as a function of time (e.g., in [6–9]). In some flow regions and for certain chemical or microphysical processes, these low-order methods could adequately capture the overall activities. Nevertheless, a more complex multidimensional analysis needs to be applied to flow regions in which the chemical or the microphysical activities could be appreciably influenced by nonuniformities in the flow condition, the thermodynamic condition, and the residence time.

This paper describes a computational fluid dynamics (CFD)-based modeling and simulation tool for complementing the limited measurement studies and addressing the sampling system issues. It accounts for and integrates fluid dynamics, chemistry, and particle microphysics relevant to aircraft emissions. The discussion proceeds as follows. Section II presents the conservation equations for the gas-phase flow. Section III describes the continuity equation for aerosol transport. Section IV discusses the implemented models of various microphysical processes such as thermophoresis, coagulation, nucleation, soot activation, condensation, and the interaction between the gaseous species and the particles. Section V presents the application of this multidimensional modeling and simulation tool. The cases reported are the first stage of a high-pressure turbine, the sampling probes, the sampling lines, and a pressure-reduction chamber. Section VI summarizes the current state of progress and suggests areas warranting future improvements.

II. Governing Equations for Gas-Phase Flow

The conservation equations for the gas-phase flow in the multiple rotating frames of reference (MRF), which are convenient for including the rotational components of the jet engine in the computational domain, are next summarized in a hybrid formulation.

Continuity equation:

$$\frac{\mathrm{d}}{\mathrm{d}t}\iiint_V \rho\,\mathrm{d}V + \iint_A \rho(\boldsymbol{u}-\boldsymbol{U}_g)\cdot\mathrm{d}\boldsymbol{A} = 0 \tag{1}$$

Species transport equation:

$$\frac{\mathrm{d}}{\mathrm{d}t}\iiint_V \rho_m \mathrm{d}V + \iint_A \rho(\boldsymbol{u}-\boldsymbol{U}_g)\cdot\mathrm{d}\boldsymbol{A} = \iint_A \rho D_{\mathrm{eff}}\nabla\left(\frac{\rho_m}{\rho}\right)\cdot\mathrm{d}\boldsymbol{A} + \iiint_V \dot{w}_m'''\mathrm{d}V \tag{2}$$

Momentum equation:

$$\frac{\mathrm{d}}{\mathrm{d}t}\iiint_V \rho\boldsymbol{u}\,\mathrm{d}V + \iint_A \rho\boldsymbol{u}(\boldsymbol{u}-\boldsymbol{U}_g)\cdot\mathrm{d}\boldsymbol{A} = -\iint_A p\,\mathrm{d}\boldsymbol{A} + \iint_A \tau\cdot\mathrm{d}\boldsymbol{A} - \iiint_V \rho\boldsymbol{\omega}_g\times\boldsymbol{u}\,\mathrm{d}V \tag{3}$$

Energy equation:

$$\frac{\mathrm{d}}{\mathrm{d}t}\iiint_V \rho E\,\mathrm{d}V + \iint_A \rho E(\boldsymbol{u}-\boldsymbol{U}_g)\cdot\mathrm{d}\boldsymbol{A} = -\iint_A p\boldsymbol{u}\cdot\mathrm{d}\boldsymbol{A} - \iint_A \boldsymbol{q}\cdot d\boldsymbol{A} + \iint_V \boldsymbol{u}\cdot\tau\cdot\mathrm{d}\boldsymbol{A} \tag{4}$$

Turbulence equations:

$$\frac{\mathrm{d}}{\mathrm{d}t}\iiint_V \rho k\,\mathrm{d}V + \iint_A \rho k(\boldsymbol{u}-\boldsymbol{U}_g)\cdot\mathrm{d}\boldsymbol{A} = S_k + \iint_A\left(\mu+\frac{\mu_t}{\sigma_k}\right)\nabla k\cdot\mathrm{d}\boldsymbol{A} \tag{5}$$

$$\frac{\mathrm{d}}{\mathrm{d}t}\iiint_V \rho\varepsilon\,\mathrm{d}V + \iint_A \rho\varepsilon(\boldsymbol{u}-\boldsymbol{U}_g)\cdot\mathrm{d}\boldsymbol{A} = S_\varepsilon + \iint_A\left(\mu+\frac{\mu_t}{\sigma_\varepsilon}\right)\nabla\varepsilon\cdot\mathrm{d}\boldsymbol{A} \tag{6}$$

where

$$\boldsymbol{q} = -\kappa\nabla T, \qquad \tau = -\tfrac{2}{3}\mu(\nabla\cdot\boldsymbol{u})\mathbf{I} + \tfrac{1}{2}\mu[\nabla\boldsymbol{u} + (\nabla\boldsymbol{u})^T]$$

V is an arbitrary control volume with control surface A, and $\boldsymbol{U}_g = \boldsymbol{\omega}_g\times\boldsymbol{r}$. For gas, the Schmidt number is about one. Different angular velocities (and even different rotating axes) are assigned to different mesh blocks or groups within the model. Balance equations for each group are expressed in the relative reference frame, but in terms of the absolute velocity (i.e., the velocity with respect to a stationary coordinate system).

III. General Dynamic Equation

A general dynamic equation (GDE) is the continuity equation for aerosol transport. Because the GDE is a nonlinear, partial integro-differential equation, analytical solutions are available for only a few special cases [10,11]. Aerosols are often described in terms of size distributions (i.e., the number of particles in a given size bin). Therefore a multiple size bin model is adopted here to approximate the aerosol GDEs. Because the governing equations for gas-phase flow are written in the MRF, the GDE will be cast in this reference system too. Furthermore, it is written in a discrete form as a population balance for each cluster or particle size, and it describes particle dynamics under the influence of various physical phenomena: convection, diffusion, coagulation, nucleation, condensation, evaporation, and external force field:

$$\frac{\mathrm{d}}{\mathrm{d}t}\iiint_V N_k\,\mathrm{d}V + \iint_A N_k(\boldsymbol{u}-\boldsymbol{U})\cdot\mathrm{d}\boldsymbol{A} = \iint_A\left(D_M + \frac{2\nu_t}{3\sqrt{C_u f_u}}\right)\nabla N_k\cdot\mathrm{d}\boldsymbol{A} + \iiint_V \left.\frac{\mathrm{d}N_k}{\mathrm{d}t}\right|_{\mathrm{micro}}\mathrm{d}V \tag{7}$$

where $k = 1,\cdots,M_B$. For noninertial particles advected by a turbulent flow, particle velocity coincides with carrier velocity. In the present work, all particles are treated as noninertial. The effective molecular (Brownian) diffusivity coefficient is defined as

$$D_M = \frac{k_B T C c_k}{3\pi\mu_g d_{p,k}} \tag{8}$$

All of the variables in the preceding equation will be defined in the following sections. The summation of microphysical processes is represented by $\mathrm{d}N_k/\mathrm{d}t|_{\mathrm{micro}}$:

$$\left.\frac{dN_k}{dt}\right|_{micro} = \left.\frac{dN_k}{dt}\right|_{drifting} + \left.\frac{dN_k}{dt}\right|_{coagulation} + \left.\frac{dN_k}{dt}\right|_{nucleation} + \left.\frac{dN_k}{dt}\right|_{cond/evap} \quad (9)$$

The first term in Eq. (9) is associated with the drifting velocity caused by external forces (e.g., the thermophoretic force, lift–dragforce, electrophoresis, and gravitational force). As for the rest of the terms, coagulation means that the particles collide and attach to each other; nucleation represents the formation of the nuclei of new particles; and condensation indicates that molecular mass transfer from the vapor phase to the particles, whereas evaporation is the reverse process of condensation.

It is further noted here that in the present work, the particle number density on a solid wall is assumed to be a fraction of the value at a point next to a solid wall, to account for the wall deposition.

IV. Models for Particle Microphysical Processes

The most important and efficient binary nucleation in the atmosphere is that of sulfuric acid and water. A free sulfuric acid molecule tends to gather water molecules around it to form hydrates. The main reason is that H_2SO_4 has extremely low saturation vapor pressure. Doyle [12] showed that even when relative humidity is less than 100%, extremely small amounts of H_2SO_4 vapor are able to induce nucleation. Within the turbine engine exhaust, major gas-phase chemical reactions will take place, and soot activation [13,14] into water condensation nuclei also occurs. If the surface of a foreign particle (e.g., soot) does participate in the gas-to-particle conversion process, the nucleation is referred to as heterogeneous. More detailed discussions on soot activation and condensation of water and sulfuric acid can be found in Wang's work [14]. The first elemental step in heterogeneous nucleation involves molecular adsorption, which is between soot and H_2SO_4 and SO_3. The nanosized aerosols will collide with each other and stick together. Such a process is called coagulation and it will change the particle size distributions.

A. Characteristics of Particles

In the present work, we assume that

1) All particles are spherical, because most of the available formulas for coagulation and condensation are for spherical particles.

2) No particle is charged, because the enhancement due to the electrical state of the soot to the collision kernel of the coagulation is negligible [9].

3) All particles are noninertial, because the majority of the particles are small enough to be considered as noninertial for the range of the conditions relevant to aviation-sourced particles.

4) Heat and momentum transfer between the carrier gas and the particles is negligible, because the particles are noninertial and the particle relaxation time is very short.

5) Gas turbulence influences the particles, but the particles do not influence the gas turbulence.

6) The particle size distribution of soot entering the postcombustor region is always prescribed.

As a consequence of these assumptions, the drifting velocity caused by the lift–drag force, electrophoresis, and gravitational force is negligible, and only the drifting velocity caused by the thermophoretic force is considered in the following analysis.

Based upon the sectional approach, the total volume range for the particles is divided into M_B bins. Using a geometric progressing factor, the volume of a particle in each bin can be calculated easily. For example, in an aerosol system, the particle size ranges from 1 nm to about 1 μm, hence, the corresponding volume ranges from 10^{-27} to 10^{-18} m^3. To cover the nine orders of magnitude volume span with 12 bins, the bins are linearly spaced on a logarithmic scale, so that $v_k = 10^{9/(12-1)} v_{k-1}$.

B. Thermophoresis

Thermophoresis arises from the temperature gradients in the carrier gas: small particles drift from hot regions toward cold regions. Brock [15] derived the following expression for the thermophoretic velocity:

$$\boldsymbol{V}_{TH_k} = \frac{-3Cc_k(k_g + c_t k_p Kn_k)}{(1 + 3c_m Kn_k)(k_p + 2k_g + 2c_t k_p Kn_k)} \left[\frac{\mu_g}{\rho_g T}\right] \nabla T \quad (10)$$

where c_m and c_t are phenomenological coefficients for which the representative values according to Brock [15] are $c_t = 2.2$ and $c_m = 1.0$. The smaller the diameter of a particle, the larger the effect of the thermophoretic force. Because the turbulent thermal diffusion discussed by Elperin et al. [16] is not included in the present model, we have

$$\left.\frac{dN_k}{dt}\right|_{drifting} = -\nabla \cdot (\boldsymbol{V}_{TH_k} N_k) \quad (11)$$

When the Knudsen number is much larger than one (i.e., $Kn_k \gg 1$; particles are much smaller than the mean free path of the carrier gas), an alternative form for the laminar thermophoretic velocity is given by [17]

$$\boldsymbol{V}_{TH_k} = \frac{-3}{4(1 + \pi\alpha/8)} \left[\frac{\mu_g}{\rho_g T}\right] \nabla T \qquad (Kn_k \gg 1) \quad (12)$$

where the negative sign indicates that the motion is in the direction of decreasing temperature, and α is the nondimensional thermal accommodation coefficient, for which the typical value is about 0.9. The thermophoretic velocity for $Kn_k \gg 1$ is independent of the particle size. Furthermore, it is nearly independent of the particle material.

C. Coagulation

Aerosol coagulation is important because it changes the size distribution and the composition of particles. Coagulation is a process in which particles in a population collide with each other and stick together to form larger particles [18]. The total volume is conserved in a coagulating aerosol ensemble. Collisions between aerosols can be initiated by gravitational settling, turbulence, and thermal (Brownian) motion. For particles smaller than 1 μm in diameter, the most important collision process is Brownian motion, which is considered in the current work. Different approaches have been developed in the past to simulate coagulation, depending upon the need and availability of computer resources. Because the model has to be incorporated into a three-dimensional CFD program, a semi-implicit scheme [19] is adopted here. All of the particles are assumed to be spherical. Soot density is less than that of carbon black and usually in the range of 1700–1800 kg/m^3, depending on the porosity of soot. Soot particles are generally small, ranging in size from 5 to 90 nm, but may be up to several micrometers in extreme cases. Soot scavenging by coagulation occurs when a small H_2SO_4–H_2O droplet collides with a larger coated soot particle.

When coagulation occurs among particles having a single particle size distribution, the change of the size distribution due to coagulation is evaluated via

$$\left.\frac{dN_k}{dt}\right|_{coag} = \frac{N_{k,t} - N_{k,t-h}}{h} \quad (13)$$

On the other hand, when coagulation occurs among particles having multiple particle size distributions, the change of the size distribution for each type of aerosol due to coagulation is evaluated via

$$\left.\frac{dN_{Yk}}{dt}\right|_{coag} = \frac{N_{Yk,t} - N_{Yk,t-h}}{h} \quad (14)$$

Details of the evaluation and definitions of the variables can be found in the Appendix.

D. Homogeneous Binary Nucleation of H_2SO_4–H_2O

The classical nucleation theory assumes that as the state of current phase is becoming unstable, a new phase is formed. It is based on the

equilibrium state of small liquid drops, or embryos, in contact with their parent vapors; some of the embryos, which become freely growing droplets, are said to be "nucleated." The theory predicts the nucleation rate as follows:

$$J_{\text{hom}} = \pi d^{*2} \beta_{\text{H}_2\text{SO}_4} N_{\text{H}_2\text{O}} \exp\left(-\frac{\Delta G^*}{R_u T}\right) \tag{15}$$

where $\pi d^{*2} \beta_{\text{H}_2\text{SO}_4} N_{\text{H}_2\text{O}}$ is a prefactor term. The change of the Gibbs free energy is a function of the number of sulfuric acid and water molecules and is represented by a two-dimensional energy surface. To become stable, a cluster will have to follow the path of least energy on this surface, thus leading to the so-called saddle point. To avoid solving iteratively to find the roots of the equations that satisfy the saddle point condition, the parameterizations of Kulmala et al. [20], updated by Vehkamäki et al. [21] for low-temperature emissions and by Vehkamäki et al. [22] for high-temperature emissions, are used here. This scheme provides the nucleation rate $J_{\text{H}_2\text{SO}_4\text{–H}_2\text{O}}$ (number of new embryos formed per second and per cubic meter) in the water/sulfuric acid mixture, and the critical cluster composition (total number of molecules and sulfuric acid mole fraction). These parameterized equations reduce the computing time by a factor of 500 compared with nonparameterized nucleation rate calculations.

1. Low-Temperature Range

The parameterized formulas are valid for temperatures between 190.15 and 305.15 K, relative humidity between 0.01 and 100%, and total sulfuric acid molecule number from 10^{10} to 10^{17} m^{-3}. The parameterization is limited to cases in which nucleation rates are between 10^{-1} and 10^{16} m$^{-3} \cdot$ s^{-1} and the critical cluster contains at least four molecules. For the cases in which the temperature is below 190.15 K, a zeroth-order extrapolation is applied to the nucleation rate; more details can be found in [21].

2. High-Temperature Range

The parameterized formulas are valid for temperatures between 300.15 and 400.15 K, relative humidity between 1 and 100%, and total sulfuric acid molecule number from 2×10^{15} to 5×10^{21} molecule/m^{-3}. The parameterization is limited to cases in which nucleation rates are between 10^5 and 10^{20} particle m$^{-3} \cdot$ s^{-1} and the critical cluster contains at least four molecules. For the cases in which the temperature is above 400.15 K, a zeroth-order extrapolation is applied to the nucleation rate. More details can be found in [22]. It is noted here that for sulfuric acid solution, experimental data are available for its surface tension when $T < 323$ K, for its density when $T < 373$ K, and for its activities when $T < 350$ K. The computed nucleation rates and other thermodynamic properties may be of greater uncertainty when the temperature is out of the experimental range.

E. Soot Activation

Because soot is hydrophobic, it must be activated to be capable of taking up water from the gas phase. Soot can be activated as water condensation nuclei by adsorption of oxidized sulfur species (H_2SO_4 and SO_3) and by scavenging (i.e., coagulation with volatile sulfate aerosols).

The fraction of soot surface due to the preceding two activation pathways is $\theta_i = \theta_{\text{ads},i} + \theta_{\text{sca},i}$, where i is the index of the size bin. Kärcher [13] presented a kinetic formula for $\theta_{\text{ads},i}$:

$$\frac{\text{d}\theta_{\text{ads},i}}{\text{d}t} = .25\alpha\bar{c}(C_{\text{SO}_3} + C_{\text{H}_2\text{SO}_4}) \times 6.02 \times 10^{23} \frac{1-\theta_i}{\sigma_0} \tag{16}$$

where α is either set to zero for $T > 420$ K or set to unity for $T \leq 420$ K, as suggested by Wang [14]. This formula, which assumes that the vapor adsorption on fresh soot takes place in the gas kinetic regime, gives the maximum adsorbed sulfur mass, and it represents the upper bound of the binary H_2SO_4–H_2O heterogeneous nucleation rate on the soot surface.

The change of surface coverage for a soot particle in size bin i by scavenging volatile H_2SO_4–H_2O droplets from size bin $j = 1$ to $j = M_B$ is determined by

$$\frac{\text{d}\theta_{\text{sca},i}}{\text{d}t} = .25 \times \sum_{j=1}^{M_B} B_{i,j} N_j d_{v,j}^2 \times \frac{1-\theta_i}{d_{s,i}^2} \tag{17}$$

where $B_{i,j}$ is the coagulation kernel between soot in size bin i and H_2SO_4–H_2O in size bin j, N_j is the number density of H_2SO_4–H_2O in size bin j, $d_{v,j}$ is the diameter of H_2SO_4–H_2O droplets in size bin j, and $d_{s,i}$ is the diameter of soot in size bin i.

The gas-phase depletion of H_2SO_4 and SO_3 due to adsorption is proportional to $1 - \theta_i$ (i.e., the available "dry" soot surface area); they are determined as follows:

$$\left.\frac{\text{d}C_{\text{SO}_3}}{\text{d}t}\right|_{\text{ads}} = -.25\alpha\bar{c}C_{\text{SO}_3} \sum_{i=1}^{M_B} N_i d_{p,i}^2 (1-\theta_i) \tag{18}$$

$$\left.\frac{\text{d}C_{\text{H}_2\text{SO}_4}}{\text{d}t}\right|_{\text{ads}} = -.25\alpha\bar{c}C_{\text{H}_2\text{SO}_4} \sum_{i=1}^{M_B} N_i d_{p,i}^2 (1-\theta_i) \tag{19}$$

where N_i is the number density of soot in size bin i. This model also accounts for the condensation of H_2SO_4–H_2O on the "wetted" soot surface area. Consequently, condensation rates onto soot particles and corresponding gas-phase depletion of H_2SO_4 and H_2O are proportional to θ_i.

Finally, using a semi-implicit method, θ_i is evaluated by

$$\theta_i^t = \frac{\theta_i^{t-h} + h(Q_{\text{ads}} + Q_{\text{sca}})}{1 + h(Q_{\text{ads}} + Q_{\text{sca}})} \tag{20}$$

where

$$Q_{\text{ads}} = .25\frac{\alpha}{\sigma_0}\bar{c}(C_{\text{SO}_3} + C_{\text{H}_2\text{SO}_4}) \times 6.02 \times 10^{23} \tag{21}$$

and

$$Q_{\text{sca}} = .25\frac{1}{d_{p,i}^2} \times \sum_{j=1}^{M_B} B_{i,j} N_j d_{p,j}^2 \tag{22}$$

F. Condensation of Water and Sulfuric Acid

If the vapor pressure of H_2SO_4 or H_2O is in excess of the equilibrium vapor pressure, condensation will occur. Condensation can occur on the liquid H_2SO_4–H_2O aerosols as well as on the liquid coating of soot surface. If the vapor pressure of H_2SO_4 is less than the equilibrium vapor pressure, then the sulfuric acid molecules will evaporate from the H_2SO_4–H_2O aerosols. However, the equilibrium vapor pressure of H_2SO_4 over the liquid droplets is so small that once H_2SO_4 molecules are condensed, they can hardly reevaporate. In contrast, H_2O will condense to and evaporate from the droplets, depending on the evolution of temperature and the partial pressure of H_2O in the carrier gas.

Following Wang and Fukuta and Walter [23], the condensational growth of $m = H_2O$ or H_2SO_4 onto particles in the size bin k is given by

$$\frac{\text{d}n_{m,k}}{\text{d}t} = 4\pi r_k D_{v,m,k}^* \left(\frac{p_m - p_{m,k,\text{sat}}}{R_u T}\right) \tag{23}$$

where $\text{d}n_{m,k}/\text{d}t$ is the rate of change in moles of species m due to condensation onto or evaporation from an aerosol with radius r_k, the modified diffusivity is

$$D_{v,m,k}^* = \frac{D_{v,m}}{r_k/(r_k + \lambda_g) + (4D_{v,m}/r_k\bar{c}_m)} \tag{24}$$

where λ_g is defined by Eq. (A9) in the Appendix. The mean thermal velocity of gaseous species m is given by

$$\bar{c}_m = \left(\frac{8R_uT}{\pi\overline{MW}_m}\right)^{1/2} \tag{25}$$

It should be noted here that when calculating the condensation on soot particles, because only the activated surface of soot can accept the diffusion of the molecules of H_2SO_4 and H_2O, the right-hand side of Eq. (23) needs to be multiplied by the fraction θ_k provided via Eq. (20). More detailed discussion on the thermodynamic properties related to the particle growth can be found in [24].

G. Effects of Microphysical Processes on Species Evolution

The conservation equations of gas-phase H_2SO_4, SO_3, and H_2O will have additional source/sink terms due to the microphysical processes described earlier, that is,

$$\frac{dC_{H_2O}}{dt} = \dot{w}'''_{H_2O} - J_{hom}n^*_{tot}(1-x^*) - \sum_{i=1}^{M_B}\frac{dn_{H_2O,i}}{dt}N_{H_2SO_4\text{-}H_2O,i} - \sum_{i=1}^{M_B}\theta_i\frac{dn_{H_2O,i}}{dt}N_{soot,i} \tag{26}$$

$$\frac{dC_{H_2SO_4}}{dt} = \dot{w}'''_{H_2SO_4} - J_{hom}n^*_{tot}x^* - \sum_{i=1}^{M_B}\frac{dn_{H_2SO_4,i}}{dt}N_{H_2SO_4\text{-}H_2O,i} - \sum_{i=1}^{M_B}\theta_i\frac{dn_{H_2SO_4,i}}{dt}N_{soot,i} - .25\alpha\bar{c}C_{H_2SO_4}\sum_{i=1}^{M_B}\pi\, d^2_{soot,i}N_{soot,i}\times(1-\theta_i) \tag{27}$$

$$\frac{dC_{SO_3}}{dt} = \dot{w}'''_{SO_3} - .25\alpha\bar{c}C_{SO_3}\sum_{i=1}^{M_B}\pi\, d^2_{soot,i}N_{soot,i}\times(1-\theta_i) \tag{28}$$

It is noted here that there also exist other models accounting for the effects of particle microphysical processes on the gas species. For example, in [25], the following relationship represents the rate of adsorption of H_2SO_4 by soot per aerosol

$$B_{H_2SO_4}(r_k) = \frac{4\pi r_k^2 D_{H_2SO_4}}{4D_{H_2SO_4}/(\beta_{c,H_2SO_4}v_{H_2SO_4}) + r_k^2/(r_k+\lambda_k)}\frac{p_{H_2SO_4}}{R_uT} \tag{29}$$

It is a function of soot particle radius, temperature, and pressure. In addition, $D_{H_2SO_4}$, β_{c,H_2SO_4}, $v_{H_2SO_4}$, and $p_{H_2SO_4}$ are the diffusivity, molecular accommodation coefficient, gas mean speed, and partial pressure of species H_2SO_4; and λ_k and r_k are the mean free path and radius of soot particle in size bin k.

Similarly, the rate of condensation of a volatile species α per wetted aerosol is given in [25] as

$$C_\alpha(r_k)[\text{mol/s}] = \frac{4\pi r_k^2 D_\alpha}{4D_\alpha/(\beta_{c,\alpha}v_\alpha) + r_k^2/(r_k+\lambda_k)}\frac{p_\alpha - p^\infty_{\alpha,k}}{R_uT} \tag{30}$$

where α is any volatile species, and $p^\infty_{\alpha,k}$ is the vapor pressure above a flat surface. Using the vapor pressure above a flat surface ignores the Kelvin effect and hence underestimates the timescale for condensation. Because the driving force for condensation is $p_\alpha - p^\infty_{\alpha,k}$, condensation will not occur if the partial pressure is below the vapor pressure. Thus, it is very important that the correct saturation vapor pressure is used.

V. Applications

The numerical platform is a NASA in-house code for simulating turbulent combustion in propulsion systems. A detailed description of this code can be found in several reports [26–28]. Its enhancements for postcombustor trace chemistry modeling and simulation are reported by Wey and Liu [29]. Under the current effort, we have further implemented the microphysical models for aerosol dynamics discussed in the previous sections into this analysis tool. In the following, the application of these models to the turbine environment as well as to the components of particle sampling system are demonstrated.

Several investigations (e.g., Lukachko et al. [8]) have shown the important role of gas-phase chemistry along the post combustor flow path in the production of sulfate and nitrate aerosol precursors. In particular, it has been suggested that multidimensional analysis needs to be applied to the high-pressure turbine section, whereas one-dimensional simulations suffice for the remaining sections of the internal gas path. It has also been known that strong modification in the temperature and pressure environment experienced by the particles in the sampling system can lead to different interpretations of the measurements aimed at characterizing the particle emissions of the exhaust. Therefore, there is a need to conduct higher-fidelity computations to complement these measurement studies and to assess the effects of sampling methodology.

Finite rate kinetic mechanisms developed for conditions intermediate between combustion and atmospheric chemistry have been used in the present work. More specifically, a mechanism involving 25 species and 74 reaction steps [30] was used for investigating the evolution of aerosol precursors in a film-cooled turbine blade [31]; later, an improved mechanism involving 29 species and 73 reaction steps [8] was used for other applications. All simulations require the specification of species concentrations along the inflow boundary of the computational domain; we have followed the approach outlined in [8] to estimate these species initial conditions.

Major sources of uncertainty in the current modeling and simulation are chemical kinetic rate parameters, coefficients used in the microphysical models, and boundary conditions for various transport equations. Because the propagations of these uncertainties in a CFD-based multidimensional modeling and simulation are highly nonlinear, an assessment of the effects of these interacting uncertainties on the calculated results calls for a comprehensive parametric study, which is beyond the scope of the current effort, but will be addressed in a future effort.

A. First Stage of a High-Pressure Turbine

Recently, two-dimensional calculations of the evolution of trace species in the first stage of a Defence Evaluation and Research Agency (DERA) high-pressure turbine (HPT1) using the CNEWT code were carried out by Lukachko et al. [8]. A relatively detailed description of the stage configuration and the specification of the inflow condition can be found in [8]. Under the present effort, the NCC code was used to calculate the evolution of trace species in the same HPT1 operating at two nominal power settings (cruise and maximum power) with similar high fuel-sulfur levels. The NCC results have been compared with the CNEWT results in terms of area-averaged quantities. In the following, results of the high-sulfur cruise case will be briefly described. Figure 1 outlines the setup of the simulations, in particular, the transfer of the solution near the exit of the nozzle guide van (NGV) to the inlet of the rotor. Because of the wake of the NGV and the rotation of the rotor, the inlet flow of the rotor is nonuniform and unsteady. Figures 2–5 present the area-averaged values of the temperature, NO, NO_2, and SO_3, respectively. These averaged values are steady in the NGV region but change with time in the rotor region. The area-averaged static temperature along the flow path decreases from 1160 to 1050 K (see Fig. 2). The area-averaged static pressure along the flow path decreases from 774,200 to 542,800 Pa (not shown). It is noted here that results of the CNEWT code were obtained by using triangular meshes and only the solutions at one time station are depicted in these figures. On the other hand, quadrilateral meshes were used in the code NCC, and solutions at several time stations are given. Depending on the variable, these temporal solutions may bunch together (e.g., temperature) or separate more clearly from each other (e.g., NO). In general, the solutions obtained by these two codes are quite comparable, except

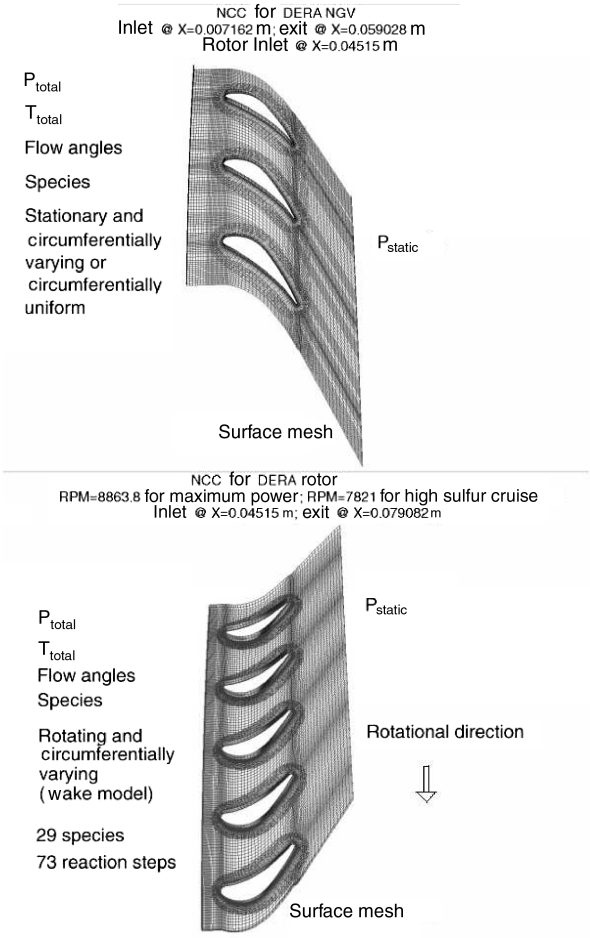

Fig. 1 Boundary-condition specification for 2-D unsteady HPT1 simulations.

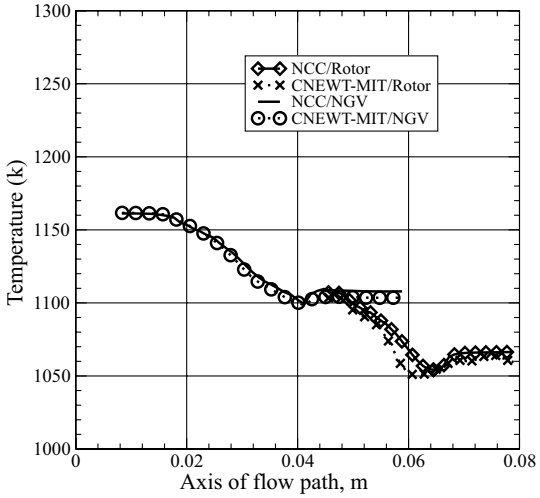

Fig. 2 Area-averaged temperature distribution along the axis of flow path for a DERA high-sulfur cruise case.

for the variable SO_3; the reason for this larger difference is not clear, nevertheless, local mesh resolutions may have played an important role. The formation of SO_3 is a complex process and is sensitive to local temperature gradient.

B. Particulate Matter Probe

Two particulate matter probes have been investigated: a low-dilution probe and a high-dilution probe. The diluent is N_2. For the low-dilution probe, the tip portion of the inlet has an inner diameter of

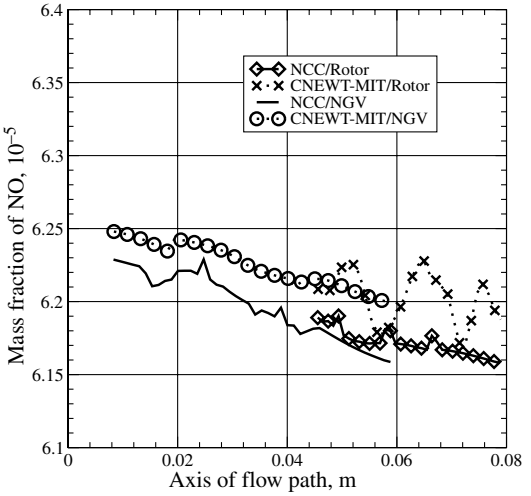

Fig. 3 Area-averaged NO distribution along the axis of flow path for a DERA high-sulfur cruise case.

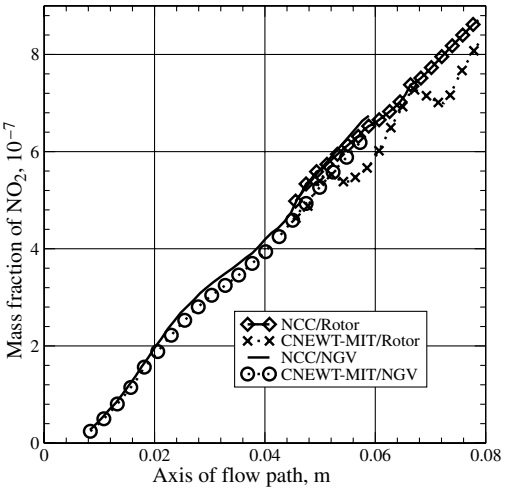

Fig. 4 Area-averaged NO2 distribution along the axis of flow path. The increase of NO_2 through the stage correlates to the decrease of temperature along the flow path.

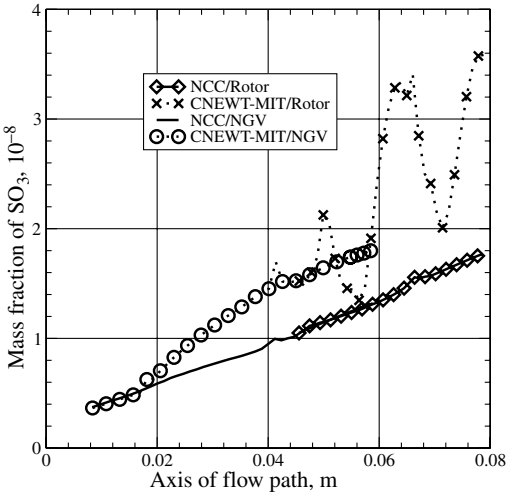

Fig. 5 Area-averaged SO_3 distribution along the axis of flow path. The increase of SO_3 through the stage correlates to the temperature decrease along the flow path.

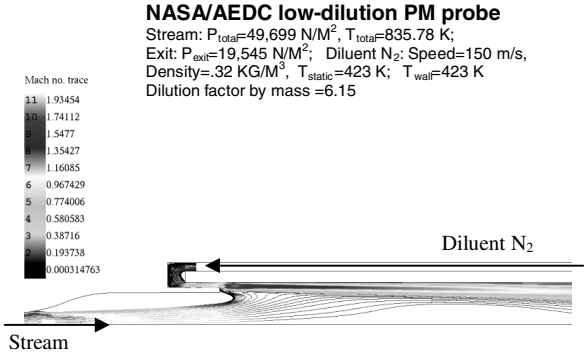

Fig. 6 Streamlines of the low-dilution PM probe.

0.0015875 m (0.0625 in.), followed by a short divergent section; the diameter at the end of the inlet is 0.0047625 m (0.1875 in.), the length of the inlet is 0.01664462 m (0.6553 in.). For the high-dilution probe, its inlet is a straight tube with an inner diameter of 0.0011176 m (0.044 in.), and a length of 0.0327 m (1.2875 in.). In the present work, the computational domain of the low-dilution probe is set to be 0.24277 m (9.558 in.) long, and the computational domain of the high-dilution probe is chosen to be 0.164 m (6.456 in.) long. The flowfield of the low-dilution probe was analyzed with an inflow total pressure of 49,699 Pa, and inflow total temperature of 835.78 K. The mass flux of the N_2 diluent is 48 $\mathrm{kg/m^2/s}$ at a temperature of 423 K. The exit pressure of the probe is set to be 19,545 Pa, and the wall temperature is set to a fixed value of 423 K. The computed dilution factor by mass is about 6.9, which is at the high end of the operation of a low-dilution probe. Figure 6 indicates that a stagnation zone appears in the downstream region of the merged inlet stream and the diluent and another flow stagnation zone sits next to the divergent wall of the inlet tube. These flow features will adversely impact the sampling functionality of the probe. Subsequently, the same flow conditions were used to evaluate the high-dilution probe. However, due to the difference in size from the low-dilution probe, the computed dilution factor by mass is now 25.8. The velocity vector fields of these two probes are compared in Fig. 7. It is evident that the high-dilution probe is much more suitable for the given sampling condition.

Because the high-dilution probe has been extensively used in the Aircraft Particle Emissions Experiment (APEX), additional simulations have been performed for the high-dilution probe. Conditions for the simulations are

1) The engine operates at 65% power setting, and the probe is located 1 m downstream of the engine exit.

2) A postcombustor trace chemistry kinetic mechanism having 29 species and 73 reaction steps is used.

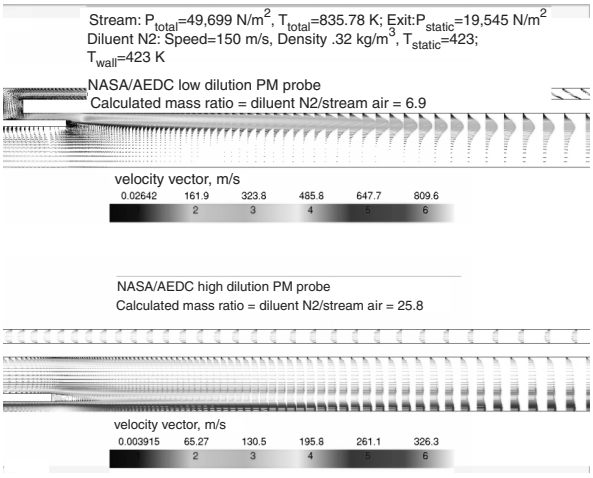

Fig. 7 Velocity vectors of two different PM probes.

3) Soot entering the probe has a number density of 9.0×10^{11} particles/$\mathrm{m^3}$ (which is in the lower range of the values measured from the in-service aircraft engines), a lognormal distribution with a median diameter of 40 nm, and a standard deviation of 1.5.

4) At the entrance of the probe, the pressure of the sampled gas is 101,350 Pa, the static temperature is 720 K, and the speed is 210 m/s; therefore, the total pressure is 112,515 Pa, and the total temperature is 742 K.

5) The static temperature of the diluent N_2 is 290 K, the diluent mass flux is 110 $\mathrm{kg/m^2/s}$, and the targeted dilution factor by mass is 24.

6) The static pressure of the mixture at the exit of the computational domain is 81,000 Pa, and the temperature of the probe wall is set to 320 K.

7) Aerosol size distribution is divided into 12 bins ($M_B = 12$); the diameter of particles in the smallest bin is 3 nm. Soot particles, H_2SO_4–H_2O droplets, and the mixture of them are included in the calculations. Consequently, a total of 72 equations are solved for each mesh cell.

Because the particle size distribution at the entrance of the probe is assumed to be lognormal, the following formula is used to discretize the continuous function into a stepwise function for size bin k:

$$N_k = \frac{N_{\text{total}}}{\sqrt{2\pi}\,\ln\sigma_g}\exp\left[-\frac{(\ln d_{p,k} - \ln d_{p,g})^2}{2\ln^2\sigma_g}\right]\frac{\Delta d_{p,k}}{d_{p,k}} \tag{31}$$

The H_2SO_4–H_2O nucleation rate depends highly on temperature, relative humidity, and H_2SO_4 concentration. The following empirical criterion [32] is used to decide whether H_2SO_4–H_2O nucleation commences:

$$C_{\text{crit}} = 0.16\exp(0.1T - 3.5\text{RH} - 27.7) \tag{32}$$

where RH is the relative humidity on a scale from 0 to 1. When the gas-phase concentration of H_2SO_4 exceeds C_{crit}, the nucleation of H_2SO_4–H_2O droplets starts. Sample results from these simulations are presented in Fig. 8. Although the number density of soot with 66-nm diameter remains essentially unchanged along the probe length, the results indicate the emergence of H_2SO_4–H_2O droplets (with a 1-nm diameter) due to nucleation.

C. Sampling Line

Three-dimensional calculations have been conducted to capture the potentially important secondary flow effects by dividing the long sampling line into multiple shorter segments. Starting from the exit plane of the high-dilution probe, a segment of the sampling line is simulated at first; the results at the exit plane of this segment are then used as the inlet profiles for the next segment, and so on. Two

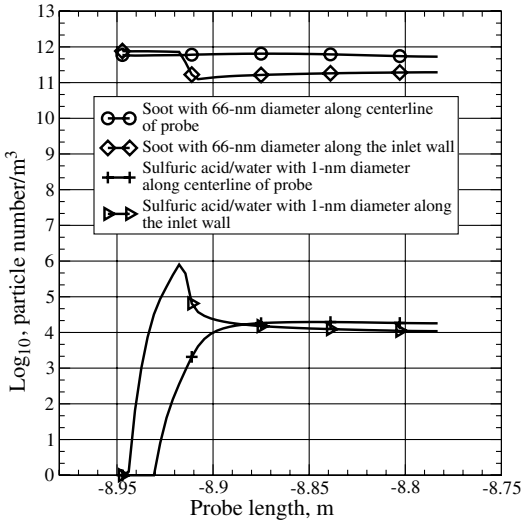

Fig. 8 Soot evolution and H_2SO_4–H_2O nucleation in a high-dilution probe.

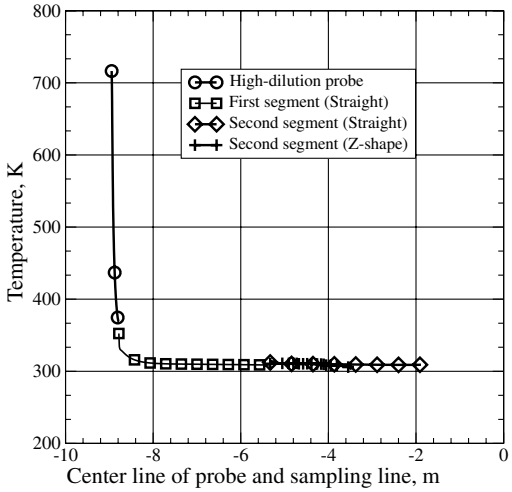

Fig. 9 Temperature distribution along the centerline of the probe and sampling lines. (There are two kinds of sampling lines. Each sampling line contains two segments: both have straight first segments; however, one is with a straight second segment and the other is with a Z-shaped second segment.)

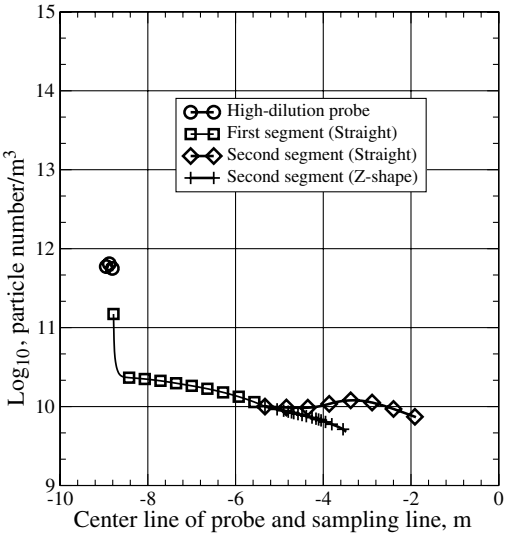

Fig. 11 Number density distribution of soot particle (33 nm) for the probe and sampling line.

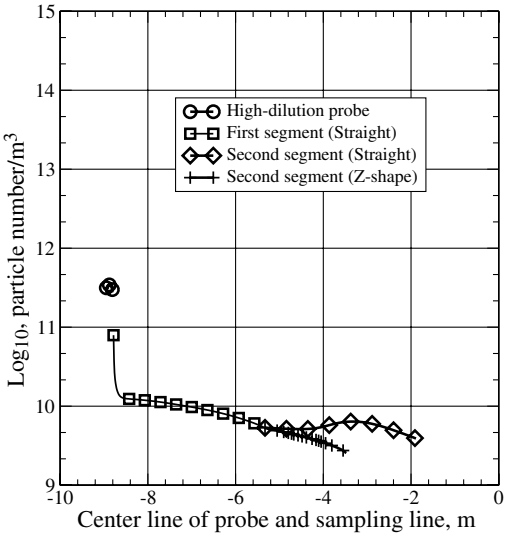

Fig. 12 Number density distribution of soot particle (66 nm) for the probe and sampling line.

configurations have been investigated. The first one consists of two segments of a simple straight tube. The second one consists of a straight tube segment followed by a Z-shaped tube segment. Figure 9 presents the temperature distribution along the centerline of the probe and along the centerline of the sampling line segments. The temperature inside the probe drops rapidly because of the dilution, whereas the temperature in the sampling line is very close to the imposed wall temperature, which is kept at 310 K. Figure 9 indicates that the static temperature along the centerlines drops from 720 to 310 K. Although not shown, it is noted here that the pressure decreases from 103,700 to 40,000 Pa along the probe and sampling line. In Fig. 10, the mass fraction distribution of species H_2SO_4 is shown. Because of a sudden expansion in volume from the end of the probe to the beginning of the sampling line, a rapid change is observed [the typical internal diameter of a sampling line is about 0.008636 m (0.34 in.), and the internal diameter at the end of the currently used high-dilution probe is 0.0063246 m (0.249 in.)]. In Fig. 11, the evolution of the soot particles with 33-nm diameter is shown. The loss of soot particles in the straight segment tends to be smaller than the loss in the Z-shaped segment. Similar behavior is observed in Fig. 12 for soot particles with 66-nm diameter. Figure 13 suggests that the process of H_2SO_4–H_2O nucleation as indicated by the emergence of droplets with 1-nm diameter starts from the inside of the probe and continues into the sampling line until the mass fraction of the gaseous H_2SO_4 levels off (see Fig. 10). The results in Fig. 14 suggest that the coagulation of H_2SO_4–H_2O droplets, as indicated by the emergence of 2-nm droplets, begins in the sampling line.

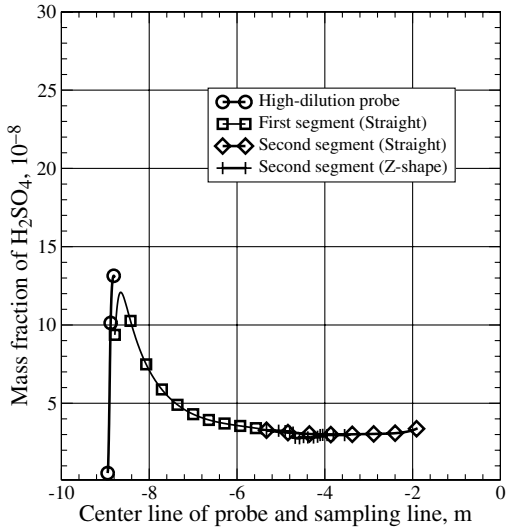

Fig. 10 Gaseous H_2SO_4 distribution for the probe and sampling lines.

D. Pressure-Reduction Chamber

The pressure of the exhaust gas at the exit of the combustor is much higher than the pressure in the ambient environment. A device that reduces the pressure of the sampled exhaust gas is often employed to meet the operating range of the particulate matter analyzers. A schematic of a typical pressure-reduction vessel is shown in Fig. 15. It is a cylinderlike device that has an inlet tube on the top and an exit tube in the bottom. The internal (inside) diameter (i.d.) of the inlet tube is denoted by a. The portion of the inlet tube inside the pressure reducer may be expanded up to 5 deg to slow down the drop of the incoming pressure and the temperature. The gap between the exit of the inlet tube and the entrance of the sample extraction tube is denoted by d. The diameter of the cylinder is denoted by S. In the current study, the internal diameter of the inlet tube is $a =$ 0.002286 m (0.09 in.) and the diameter at the exit of the inlet tube is 0.00672 m (0.2646 in.) due to a 5-deg expansion. The gap distance d is 0.0508 m (2 in.); and the i.d. of the sample extraction tube is

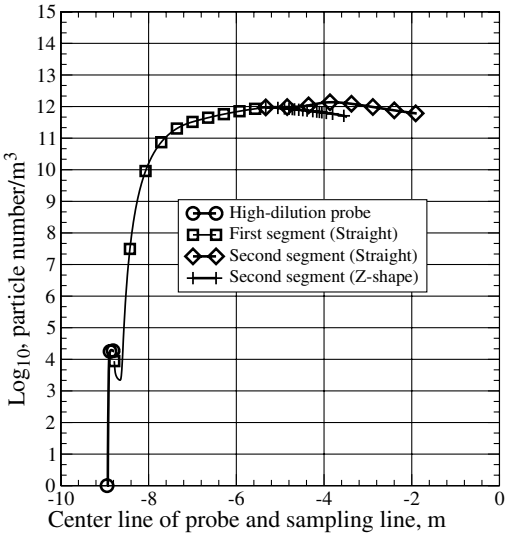

Fig. 13 Number density distribution of H_2SO_4–H_2O droplet (1 nm) for the probe and sampling line.

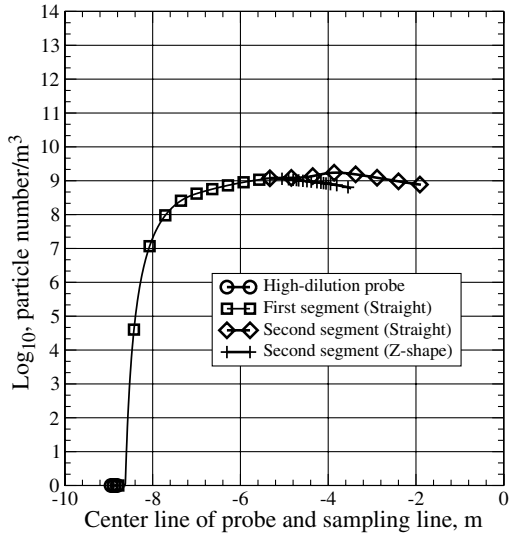

Fig. 14 Evolution of H_2SO_4–H_2O droplets (2 nm) in the probe and sampling line.

0.008636 m (0.34 in.). The diameter of the reducer is $S = 0.0762$ m (3 in.); the overall length of the domain (which includes the inlet tube, the chamber, and the sample extraction tube) is 0.889 m (35 in.).

In the current study, instead of conducting three-dimensional calculations, axisymmetric simulations have been carried out by replacing the bleeding hole with a bleeding slot having the same opening area. Two cases are presented here to show the chemical conversion and particle evolution in the device. The total pressures of the incoming gas are 448,127 Pa (65 psi) and 1,758,037 Pa (255 psi), respectively. The total temperature is set to be 485 K for both cases. The shortest flow residence time is 21 ms for the case of 448,127 Pa (65 psi) and 6.2 ms for the case of 1,758,037 Pa (255 psi). The exit pressure is set at 131,474 Pa (19.7 psi). The pressure at the bleeding location is 101,325 Pa (14.7 psi). The size distribution of the soot particles is prescribed to be lognormal, with median radius of 40 nm, modal width of 1.5, and total number density of 10^{13} particle/m^3. The chemical composition of the inlet gas and the chemical kinetic mechanism are the same as those used in the study of the particulate matter probe. The wall temperature of the inlet tube entering the vessel chamber is set to 477 K (400°F). The rest of the wall is either at a temperature of 450 K or insulated. The temperature distributions along a line that is 0.000457 m (0.018 in.) away from the center axis are shown in Fig. 16. For the 448,127 Pa (65 psi) case, the

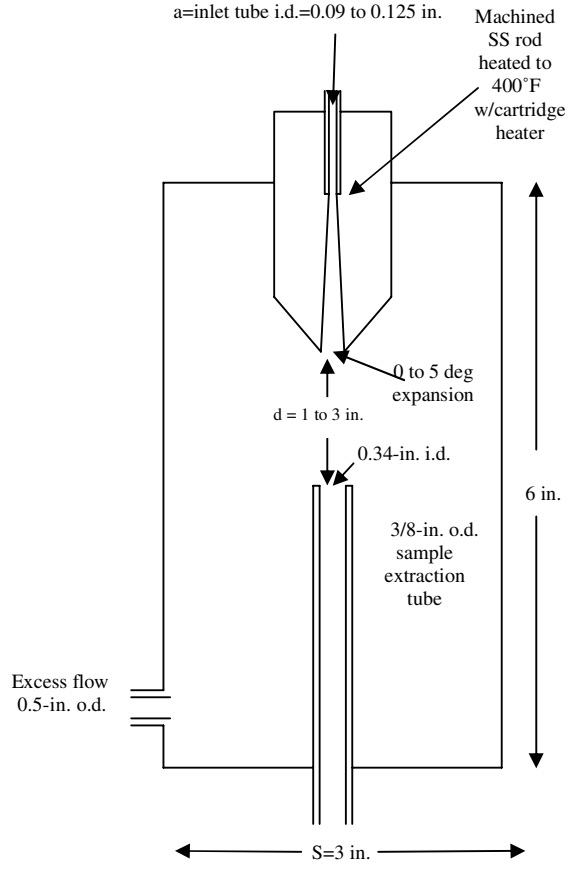

Fig. 15 Schematic of a pressure-reduction vessel.

temperature is above 450 K from the inlet to the exit, hence nucleation of H_2SO_4–H_2O droplets is not possible. For the 1,788,903 Pa (255 psi) case, the temperature has dropped to near 250 K at the end of the inlet tube. The distributions of H_2SO_4 mass fraction along the 0.000457-m (0.018-in.) line are shown in Fig. 17. The increase of the mass fraction occurs in the straight portion of the inlet tube outside of the chamber region. It also indicates that the chamber has little influence on the evolution of H_2SO_4. In Fig. 18, the number density distribution, in $\log_{10}$ scale, of the soot particles is

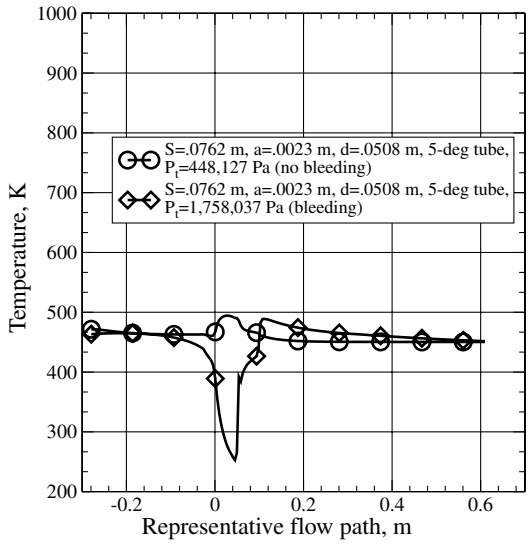

Fig. 16 Temperature distribution along a line close to the centerline of the device; *a* (0.09 in.) represents the i.d. of the inlet tube; 5 deg means that the diameter at the exit of the inlet tube is 0.00672 m (0.2646 in.), due to a 5-deg expansion; *d* (2 in.) is the gap distance; *S* (3 in.) is the diameter of the reducer; no bleeding means that the escaping valve is closed.

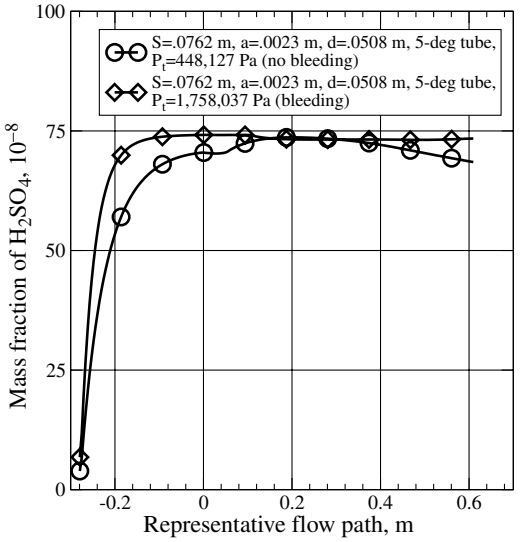

Fig. 17 H_2SO_4 distribution along a line close to the centerline of the device.

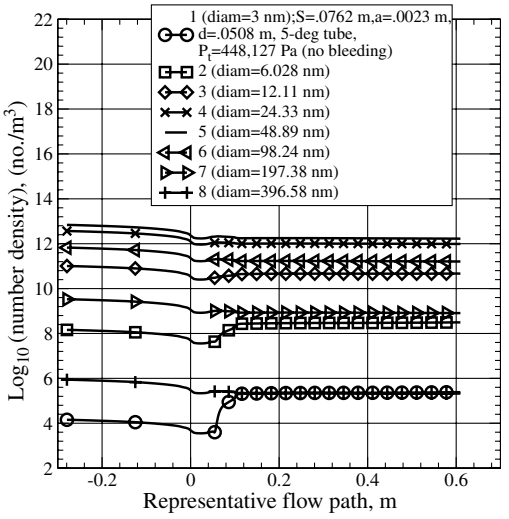

Fig. 18 Number density distribution of soot particles.

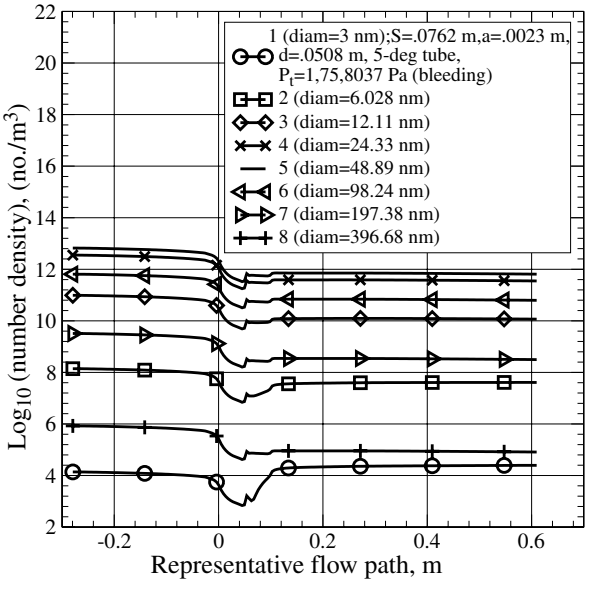

Fig. 19 Number density distribution of soot particles.

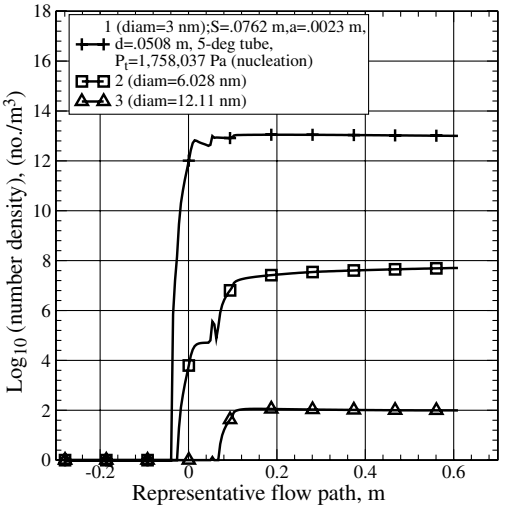

Fig. 20 Number density distribution of H_2SO_4–H_2O droplets.

shown for the 448,127 Pa (65 psi) case. The influence of the chamber on the size distribution is very mild. Figure 19 is for the 1,788,903 Pa (255 psi) case, in which the influence of the chamber on the size distribution of the soot particles is more noticeable. Figure 20 shows that due to the relatively large drop in temperature, the nucleation of H_2SO_4–H_2O droplets is significant in the case of 1,788,903 Pa (255 psi); in addition, the coagulation of smaller droplets to form larger ones also occurs.

As for the temperature and pressure ranges of the internal flows, the temperature range of these two cases are indicated in Fig. 16. Although not shown, the case of 255-psia total pressure inflow experiences a static pressure reduction from 1,427,252 Pa to 37,814 Pa, whereas the case of 65-psia total pressure inflow undergoes a static pressure reduction from 428,000 Pa to 127,500 Pa.

VI. Conclusions

To better understand the formation and subsequent development of gaseous pollutants, particulate pollutants, and their precursors in aviation-sourced emissions, it is necessary to adopt approaches that combine the use of accurate measurement and high-fidelity modeling and simulation. The development of such a CFD-based multidimensional modeling and simulation tool that accounts for and integrates fluid dynamics, chemistry, and particle microphysics relevant to aircraft emissions is elucidated in the present paper. Its capabilities are demonstrated by the results of several applications in environments representing typical postcombustor flow paths and sampling systems. This represents a first step toward the long-term goal of establishing physics-based tools that can be used to handle fundamental processes acting on length/time scales relevant to practical sampling and measurement. Obviously, the tool developed under the current effort must be further validated by data from systematic and careful parametric measurements. At the present time, measurements aimed at providing comprehensive data for the purpose of model development/improvement and validation are lacking. This is one area that needs to be strengthened by the research community. In addition to validating and further improving the existing predictive capabilities, our near-term efforts will also include modeling and simulation in the jet engine plume environment and the modeling of soot formation.

Appendix: Brownian Coagulation Among Single and Multiple Particle Distributions

I. Single Particle Size Distribution

The rate of change of a single particle size distribution due to coagulation is given by a modified Smoluchowski equation:

$$\left.\frac{dN_k}{dt}\right|_{coag} = \frac{1}{2}\sum_{j=1}^{k-1} B_{j,k-j}N_{k-j,t}N_{j,t} - N_{k,t}\sum_{j=1}^{\infty} B_{k,j}N_{j,t} \tag{A1}$$

A volume-conserving solution [19] is given by

$$\upsilon_k N_{k,t} = \frac{\upsilon_k N_{k,t-h} + h\sum_{j=1}^{k}(\sum_{i=1}^{k-1} f_{i,j,k}B_{i,j}\upsilon_i N_{i,t}N_{j,t-h})}{1 + h\sum_{j=1}^{M_B}(1 - f_{k,j,k})B_{k,j}N_{j,t-h}} \tag{A.2}$$

When two particles collide and stick together, the volume of the intermediate particle is

$$V_{i,j} = \upsilon_i + \upsilon_j \tag{A3}$$

If this volume falls between two bins, the new particle is split into adjacent bins as follows:

$$f_{i,j,k} = \begin{cases} \left[\frac{\upsilon_{k+1}-V_{i,j}}{\upsilon_{k+1}-\upsilon_k}\right]\frac{\upsilon_k}{V_{i,j}} & \upsilon_k \le V_{i,j} < \upsilon_{k+1} \qquad k < M_B \\ 1 - f_{i,j,k-1} & \upsilon_{k-1} < V_{i,j} < \upsilon_k \qquad k > 1 \\ 1 & V_{i,j} \ge \upsilon_k \qquad k = M_B \\ 0 & \text{all other cases} \end{cases} \tag{A4}$$

The generalized Brownian coagulation kernel $B_{i,j}$ for collision of particles of volume υ_i and υ_j is given by Fuchs [18]:

$$B_{i,j} = \frac{2\pi(d_i + d_j)(D_{p,i} + D_{p,j})}{\frac{d_i+d_j}{d_i+d_j+(\delta_i^2+\delta_j^2)^{1/2}} + \frac{8(D_{p,i}+D_{p,j})}{(d_i+d_j)(\bar{c}_{p,i}^2+\bar{c}_{p,j}^2)^{1/2}}} \tag{A5}$$

where the particle diffusion coefficient in the ith size bin is given by

$$D_{p,i} = \frac{k_B T C c_i}{3\pi d_{p,i}\mu_g} \tag{A6}$$

where $d_{p,i}$ is the diameter of the size-i particle. The Cunningham slip factor is defined as

$$Cc_i = 1 + Kn_i(1.257 + 0.4e^{-1.1/Kn_i}) \tag{A7}$$

where Kn_i is the Knudsen number, defined as the ratio of the mean free path of the carrier gas, λ_g, to the diameter of the size-i particle:

$$Kn_i = \frac{2\lambda_g}{d_{p,i}} \tag{A8}$$

The mean free path of the carrier gas depends upon the pressure, temperature, molecular weight of the carrier gas, and the universal gas constant; it is given by

$$\lambda_g = \frac{2\mu}{p_g[8(\overline{MW}_g/\pi R_u T)]^{1/2}} \tag{A9}$$

The mean thermal speed of a particle in size bin i is given by

$$\bar{c}_{p,i} = \left(\frac{8k_B T}{\pi m_i}\right)^{1/2} \tag{A10}$$

where δ_i represents the mean distance between the center of a sphere and a particle that has bounced from the surface of the sphere and has traveled a distance of one particle mean free path; it is given by

$$\delta_i = \frac{(d_{p,i} + \lambda_{p,i})^3 - \left(d_{p,i}^2 + \lambda_{p,i}^2\right)^{3/2}}{3d_{p,i}\lambda_{p,i}} - d_{p,i} \tag{A11}$$

The particle mean free path of a particle in size bin i is

$$\lambda_{p,i} = \frac{8D_{p,i}}{\pi\bar{c}_{p,i}} \tag{A12}$$

Finally, the change of the size distribution due to coagulation is

$$\left.\frac{dN_k}{dt}\right|_{coag} = \frac{N_{k,t} - N_{k,t-h}}{h} \tag{A13}$$

II. Multiple Particle Size Distributions

Coagulation among multiple particle distributions (e.g., among the soot particles and the H_2SO_4–H_2O liquid droplets) is also considered in the current study. Coagulation among two independent size distributions will add one more particle size distribution for the resultant particles, hence, the total number of particle size distributions becomes three. Here, the semi-implicit coagulation solution is extended to treat coagulation involving three different size distributions (e.g., $N_T = 3$), with size bins in each distribution being M_B. The resultant particle number density of the Y distribution in bin k at time t during coagulation is defined as

$$N_{Yk,t} = \frac{N_{Yk,t-h} + h(\mathrm{T}_1 + \mathrm{T}_2)}{1 + h\mathrm{T}_3} \tag{A14}$$

where

$$T_1 = \frac{1}{\upsilon_{Yk}}\sum_{M=1}^{N_T}\left[P_{Y,M}\sum_{j=1}^{k}\left(N_{Mj,t-h}\sum_{i=1}^{k-1} f_{Yi,Mj,Yk}B_{Yi,Mj}\upsilon_{Yi}N_{Yi,t}\right)\right] \tag{A15}$$

$$T_2 = \frac{1}{\upsilon_{Yk}}\sum_{M=1}^{N_T}\sum_{I=1}^{N_T}\left[Q_{I,M,Y}\sum_{j=1}^{k}\left(N_{Mj,t-h}\sum_{i=1}^{k} f_{Ii,Mj,Yk}B_{Ii,Mj}\upsilon_{Ii}N_{Ii,t}\right)\right] \tag{A16}$$

$$T_3 = \sum_{j=1}^{M_B}\left[\sum_{M=1}^{N_T}[(1 - L_{Y,M})(1 - f_{Yk,Mj,Yk}) + L_{Y,M}]B_{Yk,Mj}N_{Mj,t-h}\right] \tag{A17}$$

Term T_1 accounts for the production of larger particles in distribution Y from self-coagulation and from heterocoagulation between distribution Y and distribution $M \neq Y$. Term T_2 accounts for the production of particles in distribution Y from heterocoagulation among the other two independent distributions ($I \neq Y$ and $M \neq Y$). The first part of term T_3 accounts for self-coagulation loss in distribution Y to larger sizes, whereas the second part accounts for loss of distribution Y to all other distributions due to heterocoagulation between the Y distribution and the other distributions.

If the volume of the new particle falls between two bins, it is split into adjacent bins as follows:

$$f_{Ii,Mj,Yk} = \begin{cases} \left[\frac{\upsilon_{Yk+1}-V_{Ii,Mj}}{\upsilon_{Yk+1}-\upsilon_{Yk}}\right]\frac{\upsilon_{Yk}}{V_{Ii,Mj}} & \upsilon_{Yk} \le V_{Ii,Mj} < \upsilon_{Yk+1} \qquad k < M_B \\ 1 - f_{Ii,Mj,Yk-1} & \upsilon_{Yk-1} < V_{Ii,Mj} < \upsilon_{Yk} \qquad k > 1 \\ 1 & V_{Ii,Mj} \ge \upsilon_k \qquad k = M_B \\ 0 & \text{all other cases} \end{cases} \tag{A18}$$

The values of P, Q, and L in Eqs. (A15–A17) are either one or zero, depending on the specifics of the coagulation considered. Parameter $P_{Y,M} = 1$ if the coagulation between particles in distribution Y and in distribution M produces larger particles in distribution Y. For example, $P_{\mathrm{soot,soot}} = 1$, and $P_{\mathrm{H_2SO_4–H_2O,H_2SO_4–H_2O}} = 1$. Parameter $Q_{I,M,Y} = 1$ if the coagulation between particles in distribution I and in distribution M produces particles in distribution Y, where $I \neq M$ and $I \neq Y$. For example, $Q_{\mathrm{soot,H_2SO_4–H_2O,mix}} = 1$, and $Q_{\mathrm{H_2SO_4–H_2O,soot,mix}} = 1$. Parameter $L_{Y,M} = 1$ if the coagulation between particles in distribution Y and in distribution M does not produce particles in distribution Y. For example, $L_{\mathrm{soot,H_2SO_4–H_2O}} = 1$, and $L_{\mathrm{H_2SO_4–H_2O,soot}} = 1$.

Finally, the change of the size distribution for each type of aerosol due to coagulation is

$$\left.\frac{\mathrm{d}N_{Yk}}{\mathrm{d}t}\right|_{\mathrm{coag}} = \frac{N_{Yk,t} - N_{Yk,t-h}}{h} \tag{A19}$$

Acknowledgments

Many thanks go to Ian Waitz of the Massachusetts Institute of Technology, Richard Miake-Lye of Aerodyne Research, Inc., and Chowen Wey of the NASA John H. Glenn Research Center for their thoughtful interactions with us. We also would like to thank Robert Howard and Robert Hiers of the U.S. Air Force Arnold Engineering Development Center for providing the geometry of the dilution probes.

References

[1] Penner, J. E., Lister, D. H., Griggs, D. J., Dokken, D. J., and McFarland, M. (eds.), "Intergovernmental Panel on Climate Change (IPCC)," *Aviation and the Global Atmosphere*, Cambridge Univ. Press, New York, 1999.

[2] "Air Quality Criteria for Particulate Matter," Vols. 1, 2, U.S. Environmental Protection Agency, National Center for Environmental Assessment, Rept. EPA/600/P-99/002bF, Research Triangle Park, NC, 2004.

[3] Whitefield, P., Hagen, D., E., Brundish, K., Clague, A. R., Wilson, C. W., Miake-Lye, R. C., Brown, R. C., Wormhoudt, J., Lukachko, S. P., Chobot, A. T., Yam, C. K., and Waitz, I. A., "NASA/QinetiQ Collaborative Program, Final Report," NASA CR-2002-211900, 2002.

[4] Wilson, C. W., Petzold, A., Nyeki, S., Schumann, U., and Zeller, R., "Measurement and Prediction of Emissions of Aerosols and Gaseous Precursors from Gas Turbine Engines (PartEmis): An Overview," *Aerospace Science and Technology*, Vol. 8, No. 2, 2004, pp. 131–143.

[5] Wey, C. C., Anderson, B. E., Hudgins, C., Wey, C., Li-Jones, X., Winstead, E., Thornhill, L. K., Lobo, P., Hagen, D., Whitefield, P., Yelvington, P. E., Herdon, S. C., Onash, T. B., Miake-Lye, R. C., Wormhoudt, J., Knighton, W. B., Howard, R., Bryant, D., Corporan, E., Moses, C., Holve, D., and Dodds, W., "Aircraft Particle Emissions eXperiment (APEX)," NASA TM-2006-214382 (ARL-TR-3903), 2006.

[6] Vancassel, X., Sorokin, A., Mirabel, P., Petzold, A., and Wilson, C., "Volatile Particles Formation During PartEmis: A Modelling Study," *Atmospheric Chemistry and Physics* [online journal], Vol. 4, No. 2, 2004, pp. 439–447, www.atmos-chem-phys.net/4/439/2004/.

[7] Vouitsis, E., Ntziachristos, L., and Samaras, Z., "Modelling of Diesel Exhaust Aerosol During Laboratory Sampling," *Atmospheric Environment*, Vol. 39, No. 7, 2005, pp. 1335–1345.

[8] Lukachko, S. P., Waitz, I. A., Miake-Lye, R. C., and Brown, R. C., "Engine Design and Operational Impacts on Particulate Matter Precursor Emissions," ASME Turbo Expo 2005, Reno-Tahoe, NV, American Society of Mechanical Engineers Paper GT2005-69112, 2005.

[9] Dakhel, P. M., Lukachko, S. P., Waitz, I. A., Miake-Lye, R. C., and Brown, R. C., "Post-Combustion Evolution of Soot Properties in an Aircraft Engine," ASME Turbo Expo 2005, Reno-Tahoe, NV, American Society of Mechanical Engineers Paper GT2005-69113, 2005.

[10] Gelbard, F., and Seinfeld, J. H., "The General Dynamics Equation for Aerosols," *Journal of Colloid and Interface Science*, Vol. 68, No. 2, 1979, pp. 363–382.

[11] Peterson, T. W., Gelbard, F., and Seinfeld, J. H., "Dynamics of Source-Reinforced, Coagulating, and Condensing Aerosols," *Journal of Colloid and Interface Science*, Vol. 63, No. 2, Mar. 1978, pp. 426–445.

[12] Doyle, G. J., "Self Nucleation in the Sulfuric Acid-Water system," *Journal of Chemical Physics*, Vol. 35, Sept. 1961, pp. 795–799.

[13] Kärcher, B., "On the Potential Importance of Sulfur-Induced Activation of Soot Particles in Nascent Jet Aircraft Exhaust Plumes," *Atmospheric Research*, Vol. 46, Nos. 3–4, 1998, pp. 293–305.

[14] Wang, Z., "Numerical Modeling of Chemistry, Turbulent Mixing and Aerosol Dynamics in Near-Field Aircraft Plumes," Ph.D. Dissertation, Univ. of California at Berkeley, Berkeley, CA, 1998.

[15] Brock, J. R., "On the Theory of Thermal Forces Acting on Aerosol Particles," *Journal of Colloid Science*, Vol. 17, 1962, pp. 768–780.

[16] Elperin, T., Kleeorin, N., and Rogachevskii, I., "Turbulent Thermal Diffusion of Small Inertial Particles," *Physical Review Letters*, Vol. 76, No. 2, Jan. 1996, pp. 221–227.

[17] Waldmann, L., and Schmitt, K. H., "Thermophoresis and Diffusiophoresis of Aerosols," *Aerosol Science*, edited by C. N. Davis, Academic Press, New York, 1966, Chap. 6.

[18] Fuchs, N. A., "The Mechanics of Aerosols," Pergamon, Oxford, 1964.

[19] Jacobson, M., *Fundamentals of Atmospheric Modeling*, 2nd ed., Cambridge Univ. Press, Cambridge, England, U.K., 2005.

[20] Kulmala, M., Laaksonen, A., and Pirjola, L., "Parameterizations for Sulfuric Acid/Water Nucleation Rates," *Journal of Geophysical Research*, Vol. 103, No. D7, 1998, pp. 8301–8308.

[21] Vehkamäki, H., Kulmala, M., Napari, I., Lehtinen, K. E. J., Timmreck, C., Noppel, M., and Laaksonen, A., "An Improved Parameterization for Sulfuric Acid-Water Nucleation Rates for Tropospheric and Stratospheric Conditions," *Journal of Geophysical Research*, Vol. 107, No. D22, 2002, p. 4622.

[22] Vehkamäki, H., Kulmala, M., Lehtinen, K. E. J., and Noppel, M., "Modelling Binary Homogeneous Nucleation of Water-Sulfuric Acid Vapours: Parameterizaion for High Temperature Emissions," *Environmental Science and Technology*, Vol. 37, Aug. 2003, pp. 3392–3398.

[23] Fukuta, N., and Walter, L. A., "Kinetics of Hydrometeor Growth from a Vapor-Spherical Model," *Journal of the Atmospheric Sciences*, Vol. 27, Nov. 1970, pp. 1160–1172.

[24] Wey, T., and Liu, N.-S., "Modeling of Aerosols in Post-Combustor Flow Path and Sampling System," NASA TM-2006-214397, Sept. 2006.

[25] Brown, R. C., Miake-Lye, R. C., Anderson, M. R., Kolb, C. E., and Resch, T. J., "Aerosol Dynamics in Near-Field Aircraft Plumes," *Journal of Geophysical Research*, Vol. 101, No. D17, 1996, pp. 22,939–22,953.

[26] Chen, K.-H., Norris, A. T., Quealy, A., and Liu, N.-S., "Benchmark Test Cases for the National Combustion Code," AIAA Paper 98-3855, 1998.

[27] Ajmani, K., and Chen, K.-H., "Unsteady Flow Computations for the NCC," AIAA Paper 2001-0972, 2001.

[28] Liu, N.-S., "On the Comprehensive Modeling and Simulation of Combustion Systems," AIAA Paper 2001-0805, Jan. 2001.

[29] Wey, T., and Liu, N.-S., "Current Status of Post-Combustor Trace Chemistry Modeling and Simulation at NASA Glenn Research Center," NASA TM-2003-212184, Mar. 2003.

[30] Lukachko, S. P., Waitz, I. A., Miake-Lye, R. C., Brown, R. C., and Anderson, M. R., "Production of Sulfate Aerosol Precursors in The Turbine and Exhaust Nozzle of An Aircraft Engine," *Journal of Geophysical Research*, Vol. 103, No. D13, July 1998, pp. 16.159–16.174.

[31] Wey, T., and Liu, N.-S., "Film Cooling Flow Effects on Post-Combustor Trace Chemistry," 16th International Symposium on Air Breathing Engines, International Symposium on Air Breathing Engines (ISABE) Paper 2003-1090, 2003; also NASA TM-2003-212018, Jan. 2003.

[32] Seinfeld, J. H., and Pandis, S. N., *Atmospheric Chemistry and Physics: From Air Pollution to Climate Change*, Wiley, New York, 1998.

L. Maurice
Associate Editor